Journal of
Ceramic Science
and Technology

J. Ceram. Sci. Technol., 09 [4] 397-410 (2018)
DOI: 10.4416/JCST2018-00032
available online at: http://www.ceramic-science.com

Effect of interface oxidation on matrix multi-cracking evolution of fiber-reinforced ceramic-matrix composites at elevated temperature

L. Li*

College of Civil Aviation, Nanjing University of Aeronautics and Astronautics No.29 Yudao St., Nanjing 210016, PR China

received April 6, 2018; received in revised form May 1, 2018; accepted June 25, 2018

Abstract

In this paper, the effect of fiber/matrix interface oxidation on matrix multi-cracking evolution of fiber-reinforced ceramic-matrix composites (CMCs) is investigated using the critical matrix strain energy (CMSE) criterion. The shear-lag model combined with the fiber/matrix interface oxidation model and fiber/matrix interface debonding criterion is adopted to analyze the fiber and matrix axial stress distribution inside of the damaged composite. The relationships between matrix multi-cracking, fiber/matrix interface debonding and oxidation are established. The effects of fiber volume fraction, fiber/matrix interface shear stress, fiber/matrix interface debonded energy, oxidation temperature and oxidation time on the stress-dependent matrix multi-cracking development are discussed. Comparisons of matrix multi-cracking evolution with/without oxidation are analyzed. The experimental matrix multi-cracking development of unidirectional C/SiC, SiC/CAS, SiC/Borosilicate and mini-SiC/SiC composites with/without oxidation are predicted.

Keywords: Ceramic-matrix composites (CMCs), matrix multi-cracking, interface oxidation

I. Introduction

Ceramic materials possess high specific strength and specific modulus at elevated temperatures. But their use as structural components is severely limited because of their brittleness. Continuous fiber-reinforced ceramic-matrix composites (CMCs), based on the incorporation of fibers in ceramic matrices, however, not only exploit their attractive high-temperature strength but also reduce the propensity for catastrophic failure [1, 2]. CMC flaps for exhaust nozzles of SNECMA M53 and M88 aero engines have been used for more than a decade [3]. CMC turbine vanes have been designed and tested in aero engine environment as part of the implementation of the Ultra Efficient Engine Technology (UEET) program [4]. A CMC turbine blade has been tested for four hours by General Electric in a modified GE F414 engine, which represents the first application of CMCs in a rotating engine part. With the incorporation of CMC turbine blades in a GE90-sized engine, the overall weight can be reduced by 455 kg, which represents approximately 6 % of dry weight of a full-sized GE90 – 115 [5]. CMC combustion chamber floating wall tiles have also been tested in the aero engine environment for 30 min, with a temperature range of 1 047 ~ 1 227 °C and pressure of 2 MPa [6]. The IHI Corporation conducted the concept design of a CMC low-pressure turbine (LPT) blade with the building block approach and the failure modes and criteria are validated step by step with tests and analysis at coupon, element, sub-component and component levels [7]. The environment inside the hot-section components is harsh and the composite is typically subjected to complex thermomechanical loading, which can lead to matrix multi-cracking [8, 9]. These matrix cracks form paths for the ingress of the environment, oxidizing the fibers and leading to premature failure [10 – 14]. The density and openings of these cracks depend on the fiber architecture, fiber/matrix interface bonding intensity, applied load and environments [15, 16, 17]. It is important to develop an understanding of matrix multi-cracking damage mechanisms considering oxidation damage mechanisms [18].

Many researchers have performed experimental and theoretical investigations on matrix multi-cracking evolution of fiber-reinforced CMCs. Pryce and Smith [19] analyzed the damage evolution of unidirectional and cross-ply SiC/calcium aluminosilicate (CAS) glass-ceramic composites at the applied stress above the first matrix cracking stress determined using the Aveston-Cooper-Kelly (ACK) model [20]. Beyerle et al. [21] predicted the first matrix cracking stress and ultimate tensile strength of unidirectional SiC/CAS-II composite without considering fiber failure. Holmes and Cho [22] found that the frictional heating at the specimen surface of unidirectional SiC/CAS-II was related to the matrix cracking density at the same applied stress, stress ratio and fatigue loading frequency. Kuo and Chou [23] predicted the first matrix cracking stress of unidirectional and cross-ply CMCs using the energy balance approach. Okabe et al. [24] established the relationship between matrix cracking, fiber/matrix interface

* Corresponding author: llb451@nuaa.edu.cn

debonding and tensile stress/strain curve of unidirectional SiC/borosilicate composite. The first long matrix cracking stress coincides with the knee point of the nonlinearity in the stress/strain curve. Morscher et al. [25] established the relationships for stress-dependent matrix cracking of 2D woven Hi-Nicalon^{TM} and Sylramic-iBN SiC fiber-reinforced chemical vapor infiltrated (CVI) SiC matrix composites, which related to the stress in the load-bearing CVI SiC matrix. Morscher and Gordon [26] monitored the matrix cracking of Hi-Nicalon Type S^{TM} fibers, a boron-nitride interphase, and pre-impregnated melt-infiltrated silicon/SiC matrix composite using acoustic emission (AE) and electrical resistance (ER). AE can monitor the transverse matrix cracking and fiber break, and ER is capable of monitoring damage owing to the change in the flow of current through the material when matrix cracks form. Racle et al. [27] established the relationship between the characteristic time of 25 % total fatigue lifetime and the beginning of the matrix cracking using AE. Solti et al. [28] developed an approach of critical matrix strain energy (CMSE) criterion to analyze matrix multi-cracking evolution without considering the damage occurring in the fiber/matrix interface. Rajan and Zok [29] investigated the mechanics of a fully bridged steady-state matrix cracking in unidirectional CMCs under shear loading. In the studies mentioned above, however, the effect of fiber/matrix interface oxidation on matrix multi-cracking evolution of fiber-reinforced CMCs at elevated temperatures has not been investigated.

In this paper, the effect of fiber/matrix interface oxidation on matrix multi-cracking evolution of fiber-reinforced CMCs is investigated using the critical matrix strain energy criterion. The shear-lag model combined with the interface oxidation model and fiber/matrix interface debonding criterion is adopted to analyze the fiber and matrix axial stress distribution inside the damaged composite. The relationships between matrix multi-cracking, fiber/matrix interface debonding and oxidation are established. The effects of fiber volume fraction, fiber/matrix interface shear stress, fiber/matrix interface debonded energy, oxidation temperature and oxidation time on the stress-dependent matrix multi-cracking development are discussed. Comparisons of matrix multi-cracking evolution with/without oxidation are analyzed. The experimental matrix multi-cracking development of unidirectional C/SiC, SiC/CAS, SiC/borosilicate and mini-SiC/SiC composites with/without oxidation are predicted.

II. Theoretical Analysis

1. Stress analysis

Because of the mismatch of the axial thermal expansion coefficient between the carbon fiber and silicon carbide matrix, i.e. -0.38 × 10^{-6}/K vs 4.6 ×10^{-6}/K, microcracks unavoidably formed within the SiC matrix when the composite was cooled down from the high fabrication temperature to the ambient temperature. These processing-induced microcracks mainly exist in the surface of the material and do not propagate through the entire thickness of the composite. However, at elevated temperature, the microcracks serve as avenues for the ingress of the environment atmosphere into the composite. The oxygen reacts with carbon layer along the fiber length at a certain rate of $d\zeta/dt$, in which ζ is the length of carbon lost in each side of the crack [30].

$$\zeta = \varphi_1\left[1-\exp\left(-\frac{\varphi_2 t}{b}\right)\right] \tag{1}$$

where φ_1 and φ_2 are parameters dependent on temperature and described using the Arrhenius-type laws; and b is a delay factor considering the deceleration of reduced oxygen activity.

The composite with fiber volume fraction V_f is loaded by a remote uniform stress σ normal to the crack plane, as shown in Fig. 1. The fiber radius is r_f, and the matrix radius is R ($R = r_f/V_f^{1/2}$). The length of the unit cell is half matrix crack spacing $l_c/2$, and the interface oxidation length and interface debonded length are ζ and l_d, respectively. In the oxidation region, the fiber/matrix interface is resisted by a constant frictional shear stress τ_f; and in the debonded region, the interface is resisted by τ_i, which is higher than τ_f. For the interface debonded region, the force equilibrium equation of the fiber is given by the following equation:

$$\frac{d\sigma_f(z)}{dz} = -\frac{2\tau_i(z)}{r_f} \tag{2}$$

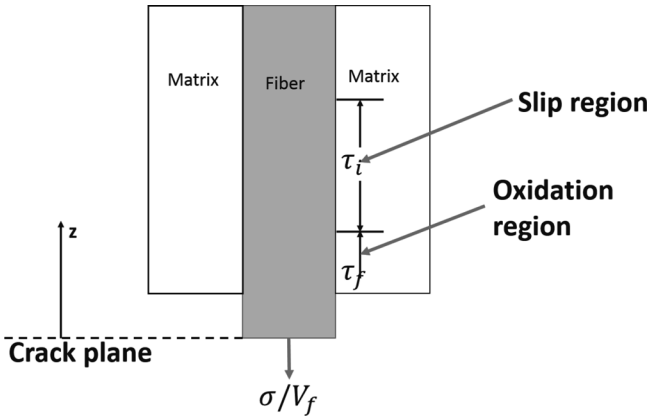

Fig. 1: The schematic of shear-lag model considering interface oxidation and debonding.

The boundary conditions at the crack plane z = 0 are given by the following equations:

$$\sigma_f(z=0) = \frac{\sigma}{V_f} \tag{3}$$

$$\sigma_m(z=0) = 0 \tag{4}$$

The total axial stresses satisfy the following equation:

$$V_f\sigma_f(z) + V_m\sigma_m(z) = \sigma \tag{5}$$

Solving Eq. (2) and (5) with the boundary conditions given by Eq. (3) and (4), and the fiber/matrix interface shear stress in the oxidation and debonded region, the fiber and matrix axial stresses in the interface oxidation and debonded region, i.e. $0<z<l_d$, can be determined with the following equations:

$$\sigma_f(z)=\begin{cases}\dfrac{\sigma}{V_f}-\dfrac{2\tau_f}{r_f}z, z\in(0,\zeta)\\ \dfrac{\sigma}{V_f}-\dfrac{2\tau_f}{r_f}\zeta-\dfrac{2\tau_i}{r_f}(z-\zeta), z\in(\zeta,l_d)\end{cases} \quad (6)$$

$$\sigma_m(z)=\begin{cases}2\dfrac{V_f}{V_m}\dfrac{\tau_f}{r_f}z, z\in(0,\zeta)\\ 2\dfrac{V_f}{V_m}\dfrac{\tau_f}{r_f}\zeta+2\dfrac{V_f}{V_m}\dfrac{\tau_i}{r_f}(z-\zeta), z\in(\zeta,l_d)\end{cases} \quad (7)$$

For the fiber/matrix bonded region (l_d<z), the fiber and matrix axial stresses and the fiber/matrix interfacial shear stress can be determined using the composite-cylinder model adopted by Budiansky-Hutchinson-Evans [31]. The fiber and matrix axial stresses and the fiber/matrix interface shear stress in the bonded region (l_d<z) can be described using the following equations:

$$\sigma_f(z)=\sigma_{fo}+\left[\frac{V_m}{V_f}\sigma_{mo}-\frac{2\tau_f}{r_f}\zeta-\frac{2\tau_i}{r_f}(l_d-\zeta)\right]\exp\left(-\rho\frac{z-l_d}{r_f}\right) \quad (8)$$

$$\sigma_m(z)=\sigma_{mo}+\left[2\frac{V_f}{V_m}\frac{\tau_f}{r_f}\zeta+2\frac{V_f}{V_m}\frac{\tau_i}{r_f}(l_d-\zeta)-\sigma_{mo}\right]\exp\left(-\rho\frac{z-l_d}{r_f}\right) \quad (9)$$

$$\tau_i(z)=\frac{\rho}{2}\left[\frac{V_m}{V_f}\sigma_{mo}-\frac{2\tau_f}{r_f}\zeta-\frac{2\tau_i}{r_f}(l_d-\zeta)\right]\exp\left(-\rho\frac{z-l_d}{r_f}\right) \quad (10)$$

where ϱ denotes the shear-lag model parameter, and

$$\sigma_{fo}=\frac{E_f}{E_c}\sigma+E_f(\alpha_c-\alpha_f)\Delta T \quad (11)$$

$$\sigma_{mo}=\frac{E_m}{E_c}\sigma+E_m(\alpha_c-\alpha_m)\Delta T \quad (12)$$

where E_f, E_m and E_c denote the fiber, matrix and composite elastic modulus, respectively; α_f, α_m and α_c denote the fiber, matrix and composite thermal expansion coefficient, respectively; and ΔT denotes the temperature difference between the fabrication temperature T_0 and testing temperature T_1 ($\Delta T=T_1-T_0$).

2. Interface debonding

When matrix cracking propagates to the fiber/matrix interface, it deflects along the interface. The fracture mechanics approach is adopted to determine the fiber/matrix interface debonded length. [32]

$$\zeta_d=\frac{F}{4\pi r_f}\frac{\partial w_f(0)}{\partial l_d}-\frac{1}{2}\int_0^{l_d}\tau_i\frac{\partial v(z)}{\partial l_d}dz \quad (13)$$

where $F=\pi r_f^2\sigma/V_f$, denotes the fiber load at the matrix cracking plane; $w_f(0)$ denotes the fiber axial displacement at the matrix cracking plane and v(z) denotes the relative displacement between the fiber and the matrix.

The fiber and matrix axial displacements of $w_f(z)$ and $w_m(z)$ are described using the following equations:

$$\begin{aligned}w_f(z)&=\int_z^{l_c/2}\frac{\sigma_f(z)}{E_f}dz\\ &=\frac{\sigma}{V_fE_f}(l_d-z)-\frac{\tau_f}{r_fE_f}(2\zeta l_d-\zeta^2-z^2)-\frac{\tau_i}{r_fE_f}(l_d-\zeta)^2+\frac{\sigma_{fo}}{E_f}\left(\frac{l_c}{2}-l_d\right)\\ &\quad+\frac{r_f}{\rho E_f}\left[\frac{V_m}{V_f}\sigma_{mo}-\frac{2\tau_f}{r_f}\zeta-\frac{2\tau_i}{r_f}(l_d-\zeta)\right]\left[1-\exp\left(-\rho\frac{l_c/2-l_d}{r_f}\right)\right]\end{aligned} \quad (14)$$

$$\begin{aligned}w_m(z)&=\int_z^{l_c/2}\frac{\sigma_m(z)}{E_m}dz\\ &=\frac{V_f\tau_f}{r_fV_mE_m}(2\zeta l_d-\zeta^2-z^2)+\frac{V_f\tau_i}{r_fV_mE_m}(l_d-\zeta)^2+\frac{\sigma_{mo}}{E_m}\left(\frac{l_c}{2}-l_d\right)\\ &\quad-\frac{r_f}{\rho E_m}\left[\sigma_{mo}-2\frac{V_f\tau_f}{r_fV_m}\zeta-2\frac{V_f\tau_i}{r_fV_m}(l_d-\zeta)\right]\left[1-\exp\left(-\rho\frac{l_c/2-l_d}{r_f}\right)\right]\end{aligned} \quad (15)$$

The relative displacement v(z) between the fiber and the matrix is described using the following equation:

$$\begin{aligned} v(x) &= \left|w_{\mathrm{f}}(z) - w_{\mathrm{m}}(z)\right| \\ &= \frac{\sigma}{V_{\mathrm{f}}E_{\mathrm{f}}}(l_{\mathrm{d}} - z) - \frac{E_{\mathrm{c}}\tau_{\mathrm{f}}}{r_{\mathrm{f}}V_{\mathrm{m}}E_{\mathrm{m}}E_{\mathrm{f}}}\left(2\zeta l_{\mathrm{d}} - \zeta^2 - z^2\right) - \frac{E_{\mathrm{c}}\tau_{\mathrm{i}}}{r_{\mathrm{f}}V_{\mathrm{m}}E_{\mathrm{m}}E_{\mathrm{f}}}(l_{\mathrm{d}} - \zeta)^2 \\ &\quad + \frac{r_{\mathrm{f}}E_{\mathrm{c}}}{\rho V_{\mathrm{m}}E_{\mathrm{m}}E_{\mathrm{f}}}\left[\sigma_{\mathrm{mo}} - 2\frac{\tau_{\mathrm{f}}}{r_{\mathrm{f}}}\zeta - 2\frac{\tau_{\mathrm{i}}}{r_{\mathrm{f}}}(l_{\mathrm{d}} - \zeta)\right]\left[1 - \exp\left(-\rho\frac{l_{\mathrm{c}}/2 - l_{\mathrm{d}}}{r_{\mathrm{f}}}\right)\right] \end{aligned} \tag{16}$$

Substituting $w_f(z=0)$ and v(z) into Eq. (13) leads to the following equation:

$$\begin{aligned} &\frac{E_{\mathrm{c}}\tau_{\mathrm{i}}^2}{r_{\mathrm{f}}V_{\mathrm{m}}E_{\mathrm{m}}E_{\mathrm{f}}}(l_{\mathrm{d}} - \zeta)^2 + \frac{E_{\mathrm{c}}\tau_{\mathrm{i}}^2}{\rho V_{\mathrm{m}}E_{\mathrm{m}}E_{\mathrm{f}}}(l_{\mathrm{d}} - \zeta) - \frac{\tau_{\mathrm{i}}\sigma}{V_{\mathrm{f}}E_{\mathrm{f}}}(l_{\mathrm{d}} - \zeta) + \frac{2E_{\mathrm{c}}\tau_{\mathrm{f}}\tau_{\mathrm{i}}}{r_{\mathrm{f}}V_{\mathrm{m}}E_{\mathrm{m}}E_{\mathrm{f}}}\zeta(l_{\mathrm{d}} - \zeta) \\ &\quad - \frac{r_{\mathrm{f}}\tau_{\mathrm{i}}\sigma}{2\rho V_{\mathrm{f}}E_{\mathrm{f}}} + \frac{E_{\mathrm{c}}\tau_{\mathrm{f}}^2}{r_{\mathrm{f}}V_{\mathrm{m}}E_{\mathrm{m}}E_{\mathrm{f}}}\zeta^2 + \frac{E_{\mathrm{c}}\tau_{\mathrm{f}}\tau_{\mathrm{i}}}{\rho V_{\mathrm{m}}E_{\mathrm{m}}E_{\mathrm{f}}}\zeta - \frac{\tau_{\mathrm{f}}\sigma}{V_{\mathrm{f}}E_{\mathrm{f}}}\zeta + \frac{r_{\mathrm{f}}V_{\mathrm{m}}E_{\mathrm{m}}\sigma^2}{4V_{\mathrm{f}}^2E_{\mathrm{f}}E_{\mathrm{c}}} - \xi_d = 0 \end{aligned} \tag{17}$$

With solving of Eq. (17), the fiber/matrix interface debonded length is determined with the following equation:

$$l_{\mathrm{d}} = \left(1 - \frac{\tau_{\mathrm{f}}}{\tau_{\mathrm{i}}}\right)\zeta + \frac{r_{\mathrm{f}}}{2}\left(\frac{V_{\mathrm{m}}E_{\mathrm{m}}\sigma}{V_{\mathrm{f}}E_{\mathrm{c}}\tau_{\mathrm{i}}} - \frac{1}{\rho}\right) - \sqrt{\left(\frac{r_{\mathrm{f}}}{2\rho}\right)^2 + \frac{r_{\mathrm{f}}V_{\mathrm{m}}E_{\mathrm{m}}E_{\mathrm{f}}}{E_{\mathrm{c}}\tau_{\mathrm{i}}^2}\xi_{\mathrm{d}}} \tag{18}$$

3. Matrix multi-cracking

Solti et al. [28] developed the critical matrix strain energy (CMSE) criterion to predict matrix multi-cracking evolution in fiber-reinforced CMCs. The concept of critical matrix strain energy presupposes the existence of an ultimate or critical strain energy. Beyond the critical value of matrix strain energy, as more energy is input into the composite with increasing applied stress, the matrix cannot support the extra load and continues to fail. The failure is assumed to consist of the formation of new cracks and fiber/matrix interface debonding, to make the total energy within the matrix remain constant and equal to its critical value.

The matrix strain energy is determined using the following equation:

$$U_{\mathrm{m}} = \frac{1}{2E_{\mathrm{m}}}\int_{A_{\mathrm{m}}}\int_0^{l_{\mathrm{c}}}\sigma_{\mathrm{m}}^2(z)\,dz\,dA_{\mathrm{m}} \tag{19}$$

where A_m is the cross-section area of matrix in the unit cell. Substituting the matrix axial stresses in Eq. (7) and (9) into Eq. (19), the matrix strain energy considering matrix multi-cracking and fiber/matrix interface partially debonding is described using the following equation:

$$\begin{aligned} U_{\mathrm{m}} = \frac{A_{\mathrm{m}}}{E_{\mathrm{m}}}\Bigg\{ &\frac{4}{3}\left(\frac{V_{\mathrm{f}}}{V_{\mathrm{m}}}\frac{\tau_{\mathrm{f}}}{r_{\mathrm{f}}}\right)^2\zeta^3 + 4\left(\frac{V_{\mathrm{f}}}{V_{\mathrm{m}}}\frac{\tau_{\mathrm{f}}}{r_{\mathrm{f}}}\right)^2\zeta^2(l_{\mathrm{d}} - \zeta) + 4\left(\frac{V_{\mathrm{f}}}{r_{\mathrm{f}}V_{\mathrm{m}}}\right)^2\tau_{\mathrm{f}}\tau_{\mathrm{i}}\zeta(l_{\mathrm{d}} - \zeta)^2 + \frac{4}{3}\left(\frac{V_{\mathrm{f}}}{V_{\mathrm{m}}}\frac{\tau_{\mathrm{i}}}{r_{\mathrm{f}}}\right)^2(l_{\mathrm{d}} - \zeta)^3 \\ &+ \sigma_{\mathrm{mo}}^2\left(\frac{l_{\mathrm{c}}}{2} - l_{\mathrm{d}}\right) + \frac{2r_{\mathrm{f}}\sigma_{\mathrm{mo}}}{\rho}\left[2\frac{V_{\mathrm{f}}}{V_{\mathrm{m}}}\frac{\tau_{\mathrm{f}}}{r_{\mathrm{f}}}\zeta + 2\frac{V_{\mathrm{f}}}{V_{\mathrm{m}}}\frac{\tau_{\mathrm{i}}}{r_{\mathrm{f}}}(l_{\mathrm{d}} - \zeta) - \sigma_{\mathrm{mo}}\right]\left[1 - \exp\left(-\rho\frac{l_{\mathrm{c}}/2 - l_{\mathrm{d}}}{r_{\mathrm{f}}}\right)\right] \\ &+ \frac{r_{\mathrm{f}}}{2\rho}\left[2\frac{V_{\mathrm{f}}}{V_{\mathrm{m}}}\frac{\tau_{\mathrm{f}}}{r_{\mathrm{f}}}\zeta + 2\frac{V_{\mathrm{f}}}{V_{\mathrm{m}}}\frac{\tau_{\mathrm{i}}}{r_{\mathrm{f}}}(l_{\mathrm{d}} - \zeta) - \sigma_{\mathrm{mo}}\right]^2\left[1 - \exp\left(-2\rho\frac{l_{\mathrm{c}}/2 - l_{\mathrm{d}}}{r_{\mathrm{f}}}\right)\right]\Bigg\} \end{aligned} \tag{20}$$

When the fiber/matrix interface completely debonds, the matrix strain energy is described using the following equation:

$$U_{\mathrm{m}}(\sigma, l_{\mathrm{c}}, l_{\mathrm{d}} = l_{\mathrm{c}}/2) = \frac{A_m}{E_{\mathrm{m}}}\left[\begin{aligned} &\frac{4}{3}\left(\frac{V_{\mathrm{f}}}{V_{\mathrm{m}}}\frac{\tau_{\mathrm{f}}}{r_{\mathrm{f}}}\right)^2\zeta^3 + 4\left(\frac{V_{\mathrm{f}}}{V_{\mathrm{m}}}\frac{\tau_{\mathrm{f}}}{r_{\mathrm{f}}}\right)^2\zeta^2(l_{\mathrm{d}} - \zeta) \\ &+4\left(\frac{V_{\mathrm{f}}}{r_{\mathrm{f}}V_{\mathrm{m}}}\right)^2\tau_{\mathrm{f}}\tau_{\mathrm{i}}\zeta(l_{\mathrm{d}} - \zeta)^2 + \frac{4}{3}\left(\frac{V_{\mathrm{f}}}{V_{\mathrm{m}}}\frac{\tau_{\mathrm{i}}}{r_{\mathrm{f}}}\right)^2(l_{\mathrm{d}} - \zeta)^3 \end{aligned}\right] \tag{21}$$

With evaluation of the matrix strain energy at a critical stress of σ_{cr}, the critical matrix strain energy of U_{crm} can be obtained. The critical matrix strain energy is described using the following equation:

$$U_{\mathrm{crm}} = \frac{1}{2}kA_{\mathrm{m}}l_0\frac{\sigma_{\mathrm{mocr}}^2}{E_{\mathrm{m}}} \tag{22}$$

where k ($k \in [0,1]$) is the critical matrix strain energy parameter; and L_0 is the initial matrix crack spacing and σ_{mocr} is determined using the following equation:

$$\sigma_{\mathrm{mocr}} = \frac{E_{\mathrm{m}}}{E_{\mathrm{c}}}\sigma_{\mathrm{cr}} + E_{\mathrm{m}}(\alpha_{\mathrm{c}} - \alpha_{\mathrm{m}})\Delta\mathrm{T} \tag{23}$$

where σ_{cr} is the critical stress corresponding to composite's proportional limit stress, i.e. the stress at which the stress-strain curve starts to deviate from linearity owing to damage accumulation of matrix cracks [35]. The critical stress is defined to be the Aveston-Cooper-Kelly matrix cracking stress [20], which was determined using the energy balance criterion, involving calculation of energy balance relationship before and after the formation of a single dominant cracking. The Aveston-Cooper-Kelly model can be used to describe long-steady-state matrix cracking stress, corresponding to the proportional limit stress of tensile stress-strain curve. The Aveston-Cooper-Kelly matrix cracking stress is determined using the following equation [20]:

$$\sigma_{cr}=\left(\frac{6V_f^2E_fE_c^2\tau_i\zeta_m}{r_fV_mE_m^2}\right)^{\frac{1}{3}}-E_c\left(\alpha_c-\alpha_m\right)\Delta T \qquad (24)$$

where ζ_m denotes the matrix fracture energy. However, as microcracks form in the matrix when CMCs are cooled down from the high fabrication temperature to room temperature, owing to thermal expansion coefficient misfit between the fiber and the matrix, these microcracks are short-matrix-cracking, and the cracking stresses of these microcracks lie in the linear region of tensile stress-strain curve [36, 37]. With increasing applied stress, matrix microcracks can propagate into long-matrix cracking. The matrix cracking stress of the Aveston-Cooper-Kelly model was used to determine the critical matrix strain energy.

The energy balance relationship to evaluate matrix multi-cracking evolution is determined using the following equation:

$$U_m\left(\sigma>\sigma_{cr},l_c,l_d\right)=U_{crm}\left(\sigma_{cr},l_0\right) \qquad (25)$$

The matrix multi-cracking evolution versus applied stress can be solved with Eq. (25) when the critical matrix cracking stress of σ_{cr} and the fiber/matrix interface debonded length of l_d are determined with Eq. (18) and (24).

III. Discussion

The ceramic composite system of SiC/CAS is used for the case study and its material properties are given by [21]: V_f =30 %, E_f = 200 GPa, E_m = 97 GPa, r_f = 7.5 μm, ζ_m = 6 J/m^2, ζ_d = 0.8 J/m^2, τ_i = 20 MPa, α_f = 4×10^{-5}/K, α_m = 5×10^{-5}/K, ΔT = -1000 K.

1. *Effect of fiber volume fraction*

The matrix cracking density, fiber/matrix interface debonded length (l_d/r_f), interface debonding ratio ($2l_d/l_c$) and interface oxidation ratio (ζ/l_d) corresponding to different fiber volume fractions (i.e. V_f=30 % and 35 %) are shown in Fig. 2.

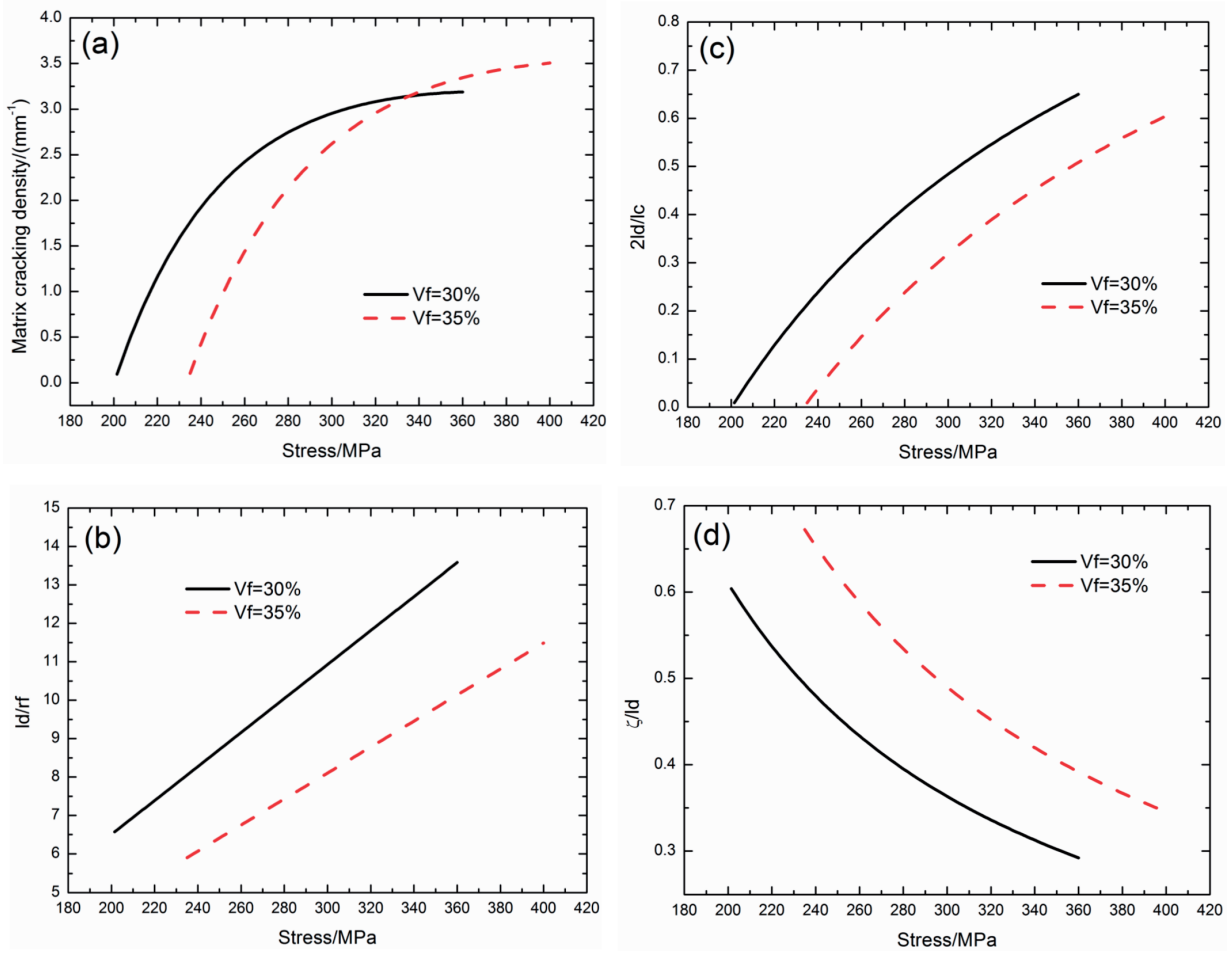

Fig. 2: The effect of fiber volume fraction (i.e. V_f = 30 % and 35 %) on (a) the matrix cracking density versus applied stress curves; (b) the fiber/matrix interface debonded length (l_d/r_f) versus applied stress curves; (c) the fiber/matrix interface debonding ratio ($2l_d/l_c$) versus applied stress curves; and (d) the fiber/matrix interface oxidation ratio (ζ/l_d) versus applied stress curves.

When the fiber volume fraction is V_f=30 %, the matrix cracking density increases from 0.09/mm at the first matrix cracking stress of 201 MPa to 3.1/mm at the saturation matrix cracking stress of 360 MPa; the fiber/matrix interface debonded length (l_d/r_f) increases from 6.5 to 13.5; the fiber/matrix interface debonding ratio ($2l_d/l_c$) increases from 0.9 % to 64.9 %; and the fiber/matrix interface oxidation ratio (ζ/l_d) decreases from 60 % to 29 %.

When the fiber volume fraction is V_f = 35 %, the matrix cracking density increases from 0.1/mm at the first matrix cracking stress of 235 MPa to 3.5/mm at the saturation matrix cracking stress of 400 MPa; the fiber/matrix interface debonded length (l_d/r_f) increases from 5.9 to 11.4; the fiber/matrix interface debonding ratio ($2l_d/l_c$) increases from 0.9 % to 60.3 %; and the fiber/matrix interface oxidation ratio (ζ/l_d) decreases from 67.2 % to 34.5 %.

With increasing fiber volume fraction, the first matrix cracking stress, matrix saturation cracking stress and matrix cracking density increase; the fiber/matrix interface debonded length and interface debonding ratio decrease; and the interface oxidation ratio increases.

2. *Effect of fiber/matrix interface shear stress*

The matrix cracking density, fiber/matrix interface debonded length (l_d/r_f), interface debonding ratio ($2l_d/l_c$) and interface oxidation ratio (ζ/l_d) corresponding to different fiber/matrix interface shear stress of τ_i = 10 and 15 MPa are shown in Fig. 3.

When the fiber/matrix interface shear stress is τ_i = 10 MPa, the matrix cracking density increases from 0.12/mm at the first matrix cracking stress of 147 MPa to 2.7/mm at the saturation matrix cracking stress of 238 MPa; the fiber/matrix interface debonded length (l_d/r_f) increases from 4.4 to 19.6; the fiber/matrix interface debonding ratio ($2l_d/l_c$) increases from 0.8 % to 81.9 %; and the fiber/matrix interface oxidation ratio (ζ/l_d) decreases from 90.2 % to 20.1 %.

When the fiber/matrix interface shear stress is τ_i =15 MPa, the matrix cracking density increases from 0.09/mm at the first matrix cracking stress of 177 MPa to 2.9/mm at the saturation matrix cracking stress of 315 MPa; the fiber/matrix interface debonded length (l_d/r_f) increases from 6.0 to 14.4; the fiber/matrix interface debonding ratio ($2l_d/l_c$) increases from 0.9 % to 63.9 %; and the fiber/matrix interface oxidation ratio (ζ/l_d) decreases from 65.8 % to 27.5 %.

With increasing fiber/matrix interface shear stress of τ_i, the first matrix cracking stress, matrix saturation cracking stress and matrix cracking density increase; the fiber/matrix interface debonded length and interface debonding ratio decrease; and the fiber/matrix interface oxidation ratio increases.

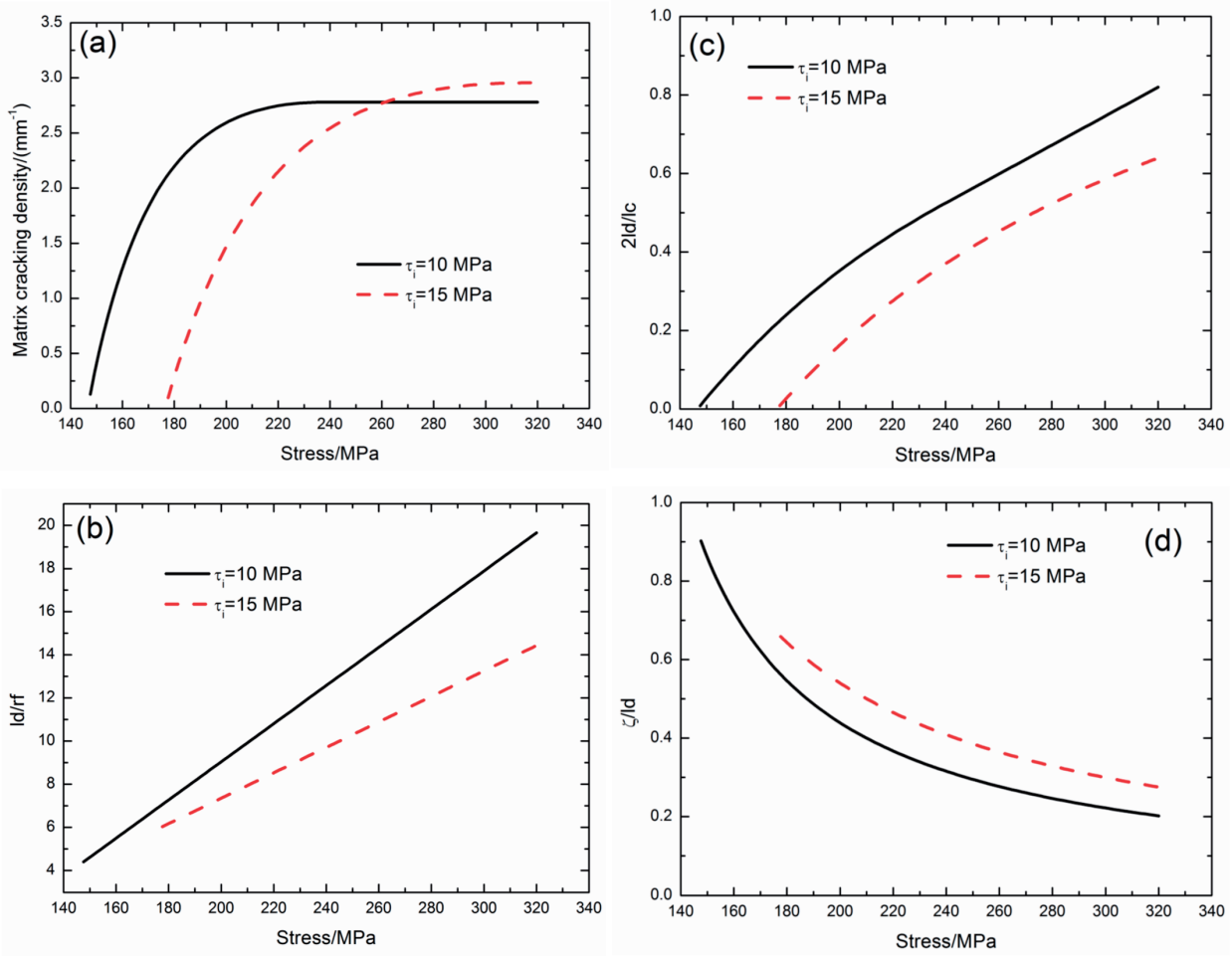

Fig. 3: The effect of fiber/matrix interface shear stress (i.e. τ_i = 10 and 15 MPa) on (a) the matrix cracking density versus applied stress curves; (b) the fiber/matrix interface debonded length (l_d/r_f) versus applied stress curves; (c) the fiber/matrix interface debonding ratio ($2l_d/l_c$) versus applied stress curves; and (d) the fiber/matrix interface oxidation ratio (ζ/l_d) versus applied stress curves.

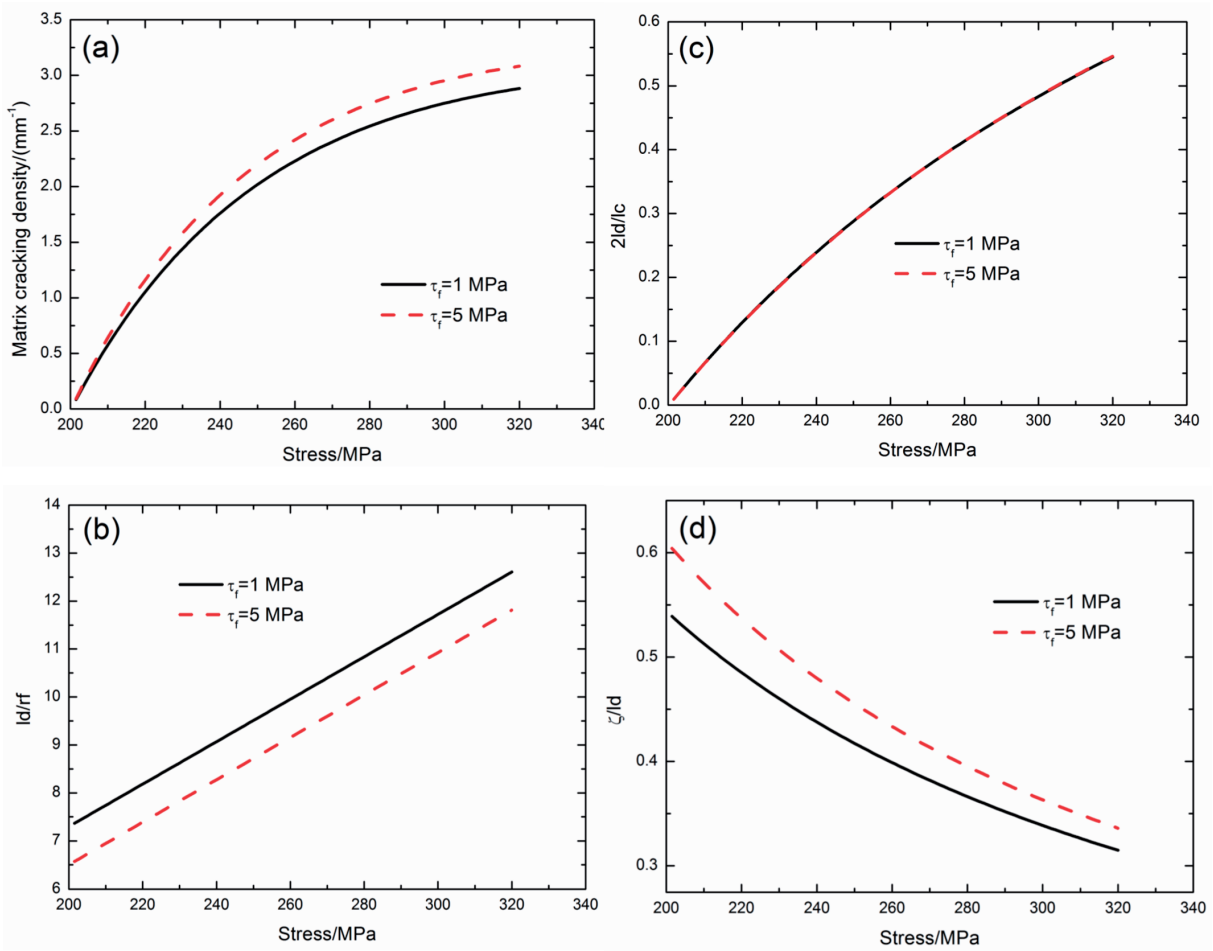

Fig. 4: The effect of fiber/matrix interface shear stress (i.e. τ_f = 1 and 5 MPa) on (a) the matrix cracking density versus applied stress curves; (b) the fiber/matrix interface debonded length (l_d/r_f) versus applied stress curves; (c) the fiber/matrix interface debonding ratio ($2l_d/l_c$) versus applied stress curves; and (d) the fiber/matrix interface oxidation ratio (ζ/l_d) versus applied stress curves.

The matrix cracking density, fiber/matrix interface debonded length (l_d/r_f), interface debonding ratio ($2l_d/l_c$) and interface oxidation ratio (ζ/l_d) corresponding to different fiber/matrix interface shear stress of τ_f= 1 and 5 MPa are shown in Fig. 4.

When the fiber/matrix interface shear stress is τ_f = 1 MPa, the matrix cracking density increases from 0.08/mm at the first matrix cracking stress of 201 MPa to 2.8/mm at the saturation matrix cracking stress of 320 MPa; the fiber/matrix interface debonded length (l_d/r_f) increases from 7.3 to 12.6; the fiber/matrix interface debonding ratio ($2l_d/l_c$) increases from 0.93 % to 54.5 %; and the fiber/matrix interface oxidation ratio (ζ/l_d) decreases from 53.9 % to 31.5 %.

When the fiber/matrix interface shear stress is τ_f = 5 MPa, the matrix cracking density increases from 0.09/mm at the first matrix cracking stress of 201 MPa to 3.0/mm at the saturation matrix cracking stress of 320 MPa; the fiber/matrix interface debonded length (l_d/r_f) increases from 6.5 to 11.8; the fiber/matrix interface debonding ratio ($2l_d/l_c$) increases from 0.92 % to 54.6 %; and the fiber/matrix interface oxidation ratio (ζ/l_d) decreases from 60.4 % to 33.6 %.

With increasing fiber/matrix interface shear stress of τ_f, the matrix cracking density increases; the fiber/matrix interface debonded length decreases; and the fiber/matrix interface oxidation ratio increases.

3. *Effect of fiber/matrix interface debonded energy*

The matrix cracking density, fiber/matrix interface debonded length (l_d/r_f), interface debonding ratio ($2l_d/l_c$) and interface oxidation ratio (ζ/l_d) corresponding to different fiber/matrix interface debonded energy of ξ_d = 0.5 and 1.0 J/m^2 are shown in Fig. 5.

When the fiber/matrix interface debonded energy is ξ_d = 0.5 J/m^2, the matrix cracking density increases from 0.08/mm at the first matrix cracking stress of 201 MPa to 2.9/mm at the saturation matrix cracking stress of 320 MPa; the fiber/matrix interface debonded length (l_d/r_f) increases from 7.6 to 12.9; the fiber/matrix interface debonding ratio ($2l_d/l_c$) increases from 0.95 % to 56.3 %; and the fiber/matrix interface oxidation ratio (ζ/l_d) decreases from 51.6 % to 30.7 %.

When the fiber/matrix interface debonded energy is ξ_d =1.0 J/m^2, the matrix cracking density increases from 0.1/mm at the first matrix cracking stress of 201 MPa to 3.2/mm at the saturation matrix cracking stress of 320 MPa; the fiber/matrix interface debonded length (l_d/r_f) increases from 5.9 to 11.2; the fiber/matrix interface debonding ratio ($2l_d/l_c$) increases from 0.9 % to 53.7 %; and the fiber/matrix interface oxidation ratio (ζ/l_d) decreases from 66.8 % to 35.4 %.

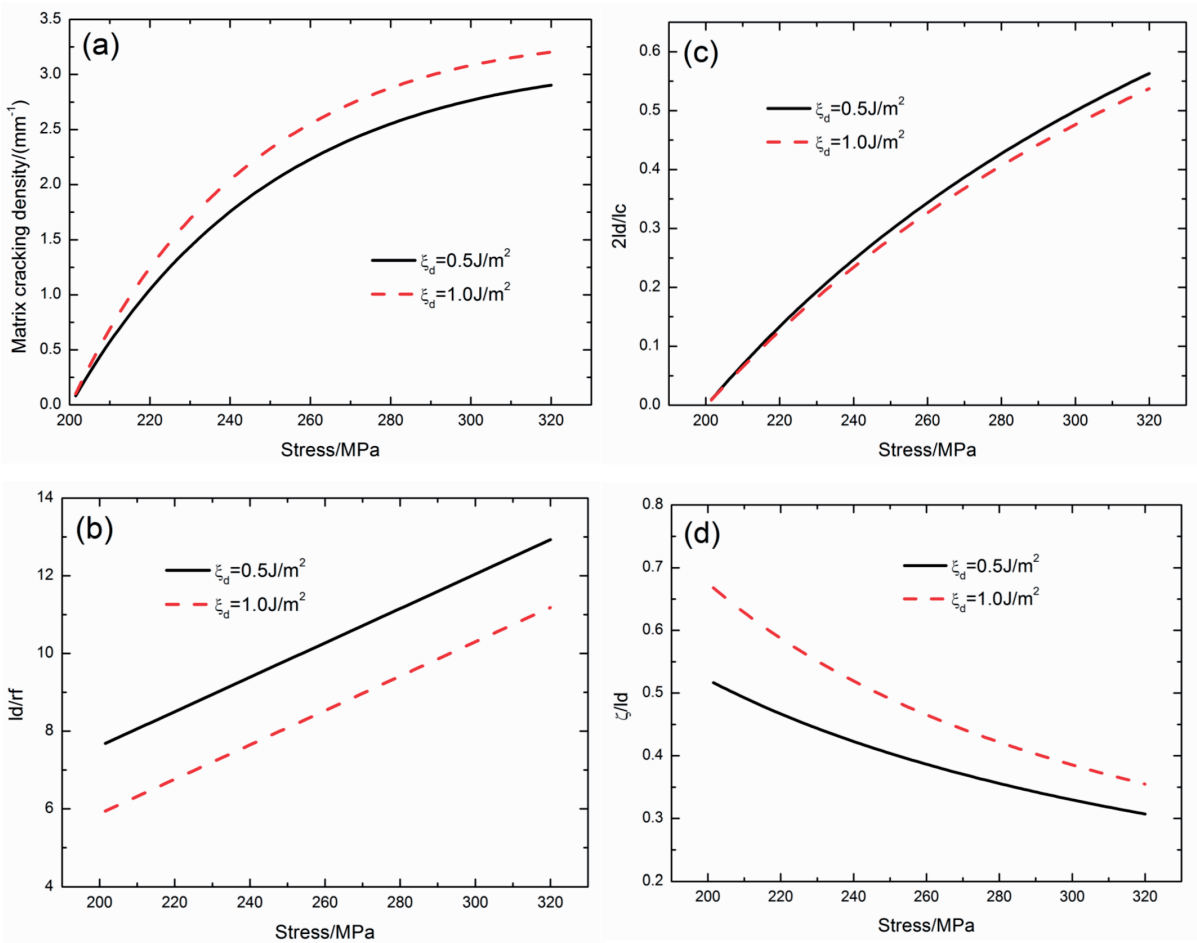

Fig. 5: The effect of fiber/matrix interface debonded energy (i.e. ξ_d = 0.5 and 1.0 J/m^2) on (a) the matrix cracking density versus applied stress curves; (b) the fiber/matrix interface debonded length (l_d/r_f) versus applied stress curves; (c) the fiber/matrix interface debonding ratio ($2l_d/l_c$) versus applied stress curves; and (d) the fiber/matrix interface oxidation ratio (ζ/l_d) versus applied stress curves.

With increasing fiber/matrix interface debonded energy, the matrix cracking density increases; the fiber/matrix interface debonded length and interface debonding ratio decrease; and the fiber/matrix interface oxidation ratio increases.

4. *Effect of oxidation temperature*

The matrix cracking density, fiber/matrix interface debonded length (l_d/r_f), interface debonding ratio ($2l_d/l_c$) and interface oxidation ratio (ζ/l_d) corresponding to different oxidation temperature of Temp = 600 °C and 900 °C are shown in Fig. 6.

When the oxidation temperature is Temp = 600 °C, the matrix cracking density increases from 0.14/mm at the first matrix cracking stress of 201 MPa to 3.9/mm at the saturation matrix cracking stress of 320 MPa; the fiber/matrix interface debonded length (l_d/r_f) increases from 4.0 to 9.2; the fiber/matrix interface debonding ratio ($2l_d/l_c$) increases from 0.8 % to 55 %; and the fiber/matrix interface oxidation ratio (ζ/l_d) decreases from 14.8 % to 6.4 %.

When the oxidation temperature is Temp = 900 °C, the matrix cracking density increases from 0.06/mm at the first matrix cracking stress of 201 MPa to 2.4/mm at the saturation matrix cracking stress of 320 MPa; the fiber/matrix interface debonded length (l_d/r_f) increases from 9.6 to 14.8; the fiber/matrix interface debonding ratio ($2l_d/l_c$) increases from 0.95% to 54.3 %; and the fiber/matrix interface oxidation ratio (ζ/l_d) decreases from 83.4 % to 53.9 %.

With increasing oxidation temperature, the matrix cracking density decreases; the fiber/matrix interface debonded length increases; and the fiber/matrix interface oxidation ratio increases.

5. *Effect of oxidation time*

The matrix cracking density, fiber/matrix interface debonded length (l_d/r_f), interface debonding ratio ($2l_d/l_c$) and interface oxidation ratio (ζ/l_d) corresponding to different oxidation times of t = 1 and 2 h are shown in Fig. 7.

When the oxidation time is t =1 h, the matrix cracking density increases from 0.09/mm at the first matrix cracking stress of 201 MPa to 3.0/mm at the saturation matrix cracking stress of 320 MPa; the fiber/matrix interface debonded length (l_d/r_f) increases from 6.5 to 11.8; the fiber/matrix interface debonding ratio ($2l_d/l_c$) increases from 0.9 % to 54.6 %; and the fiber/matrix interface oxidation ratio (ζ/l_d) decreases from 60.4 % to 33.6 %.

When the oxidation time is t = 2 h, the matrix cracking density increases from 0.06/mm at the first matrix cracking stress of 201 MPa to 2.4/mm at the saturation matrix cracking stress of 320 MPa; the fiber/matrix interface debonded length (l_d/r_f) increases from 9.5 to 14.7; the fiber/matrix interface debonding ratio ($2l_d/l_c$) increases from 0.95 % to 54.3 %; and the fiber/matrix interface oxidation ratio (ζ/l_d) decreases from 83.1 % to 53.6 %.

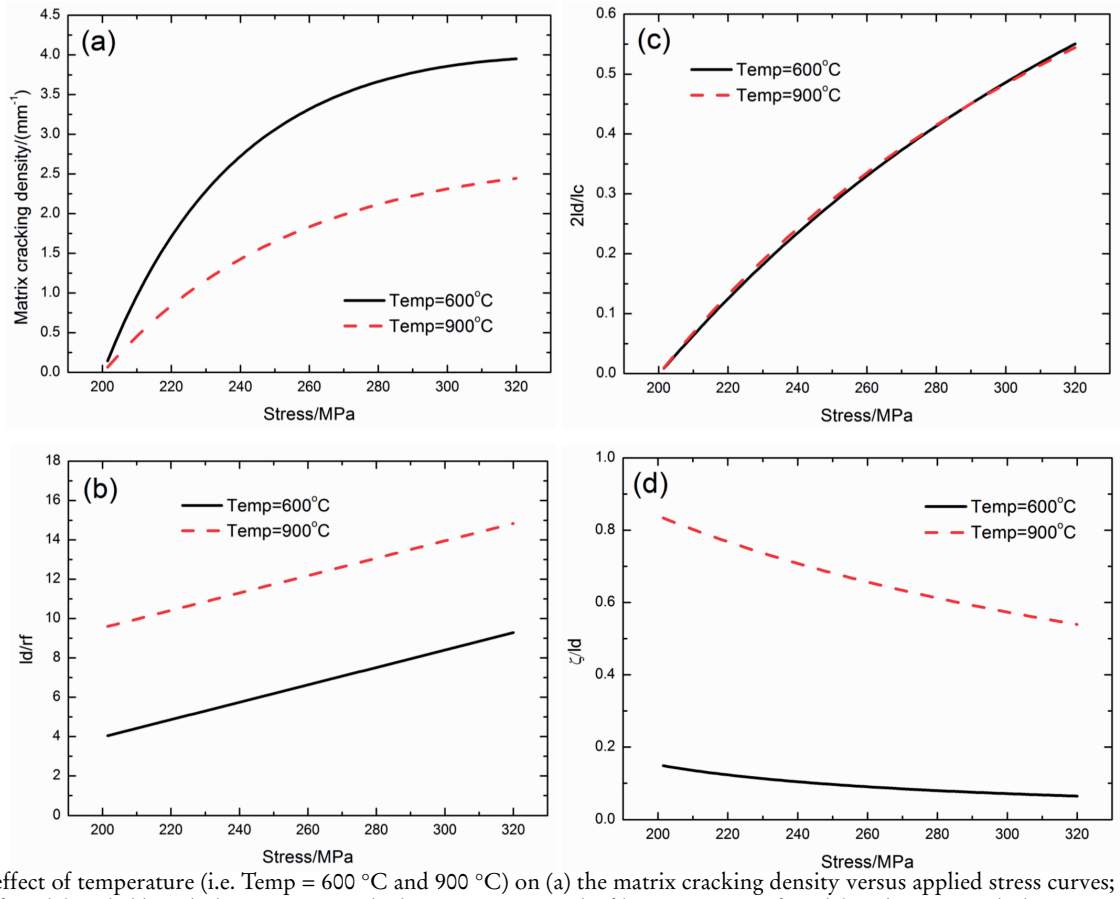

Fig. 6: The effect of temperature (i.e. Temp = 600 °C and 900 °C) on (a) the matrix cracking density versus applied stress curves; (b) the fiber/matrix interface debonded length (l_d/r_f) versus applied stress curves; (c) the fiber/matrix interface debonding ratio ($2l_d/l_c$) versus applied stress curves; and (d) the fiber/matrix interface oxidation ratio (ζ/l_d) versus applied stress curves.

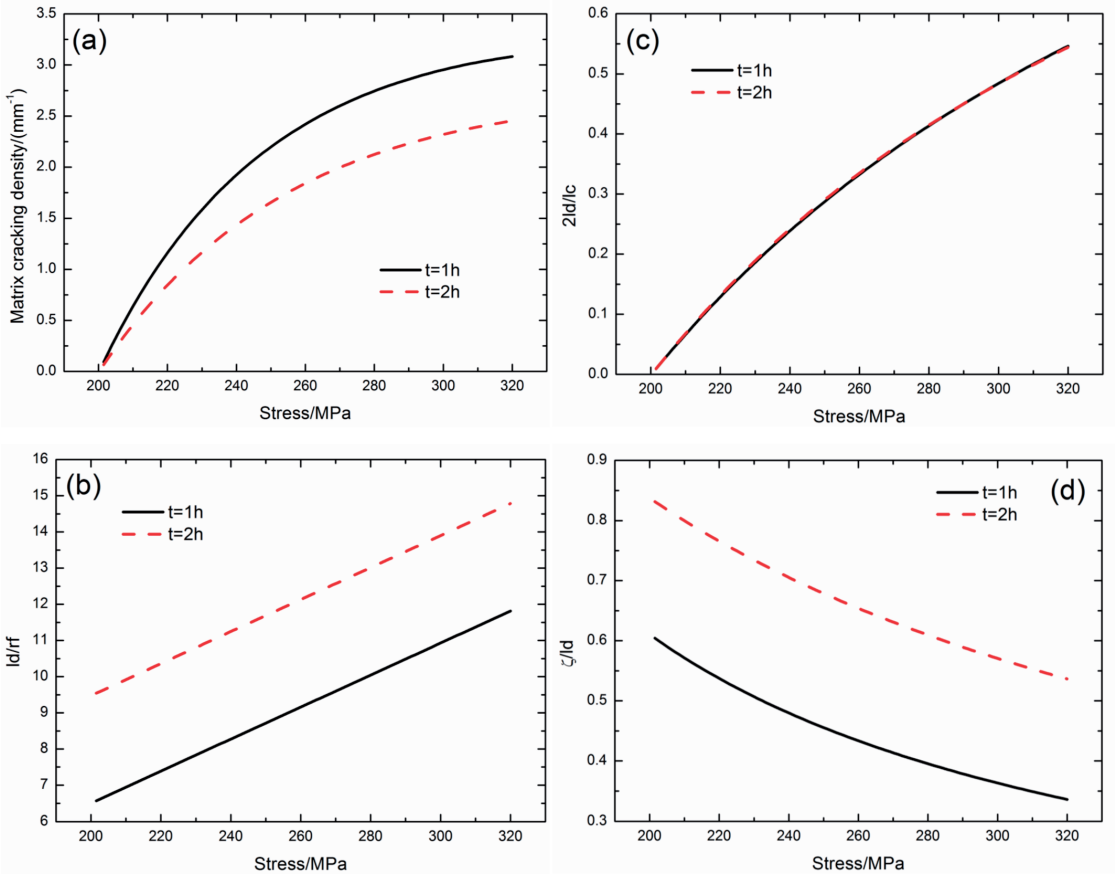

Fig. 7: The effect of oxidation time (i.e. t = 1 h and 2 h) on (a) the matrix cracking density versus applied stress curves; (b) the fiber/matrix interface debonded length (l_d/r_f) versus applied stress curves; (c) the fiber/matrix interface debonding ratio ($2l_d/l_c$) versus applied stress curves; and (d) the fiber/matrix interface oxidation ratio (ζ/l_d) versus applied stress curves.

With increasing oxidation time, the matrix cracking density decreases; the fiber/matrix interface debonded length increases; and the fiber/matrix interface oxidation ratio increases.

6. Comparisons with/without oxidation

Comparisons of matrix cracking density and fiber/matrix interface debonding ratio with and without oxidation are shown in Fig. 8.

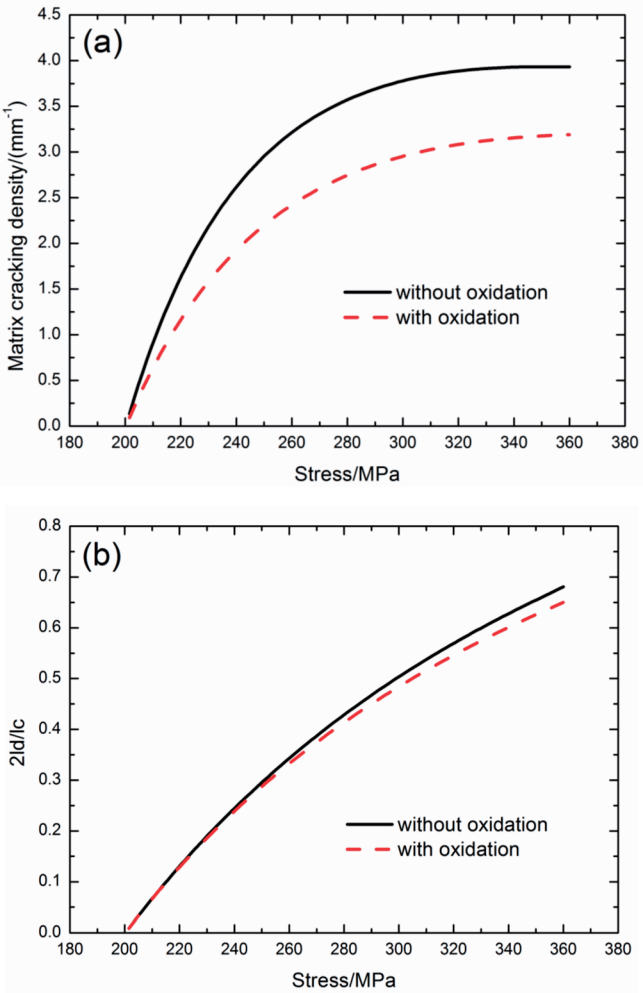

Fig. 8: The comparisons of with/without oxidation for (a) matrix cracking density versus applied stress curves; and (b) the fiber/matrix interface debonding ratio ($2l_d/l_c$) versus applied stress curves.

Without considering fiber/matrix interface oxidation, the matrix cracking density increases from 0.13/mm at the first matrix cracking stress of 201 MPa to 3.9/mm at the saturation matrix cracking stress of 360 MPa; and the fiber/matrix interface debonding ratio ($2l_d/l_c$) increases from 0.92 % to 68 %.

With consideration of fiber/matrix interface oxidation, the matrix cracking density increases from 0.09/mm at the first matrix cracking stress of 201 MPa to 3.1/mm at the saturation matrix cracking stress of 360 MPa; and the fiber/matrix interface debonding ratio ($2l_d/l_c$) increases from 0.92 % to 64.9 %.

With fiber/matrix interface oxidation, the matrix cracking density and the fiber/matrix interface debonding ratio decrease.

IV. Experimental Comparisons

The experimental and theoretical matrix cracking density, fiber/matrix interface debonded length ($2l_d/l_c$) and broken fibers fraction versus applied stress for different CMCs, i.e. unidirectional C/SiC, SiC/CAS [19], SiC/borosilicate [24] and mini-SiC/SiC [38] composites are predicted using the present analysis, as shown in Fig. 9 ~ 13. The material properties of CMCs are listed in Table 1.

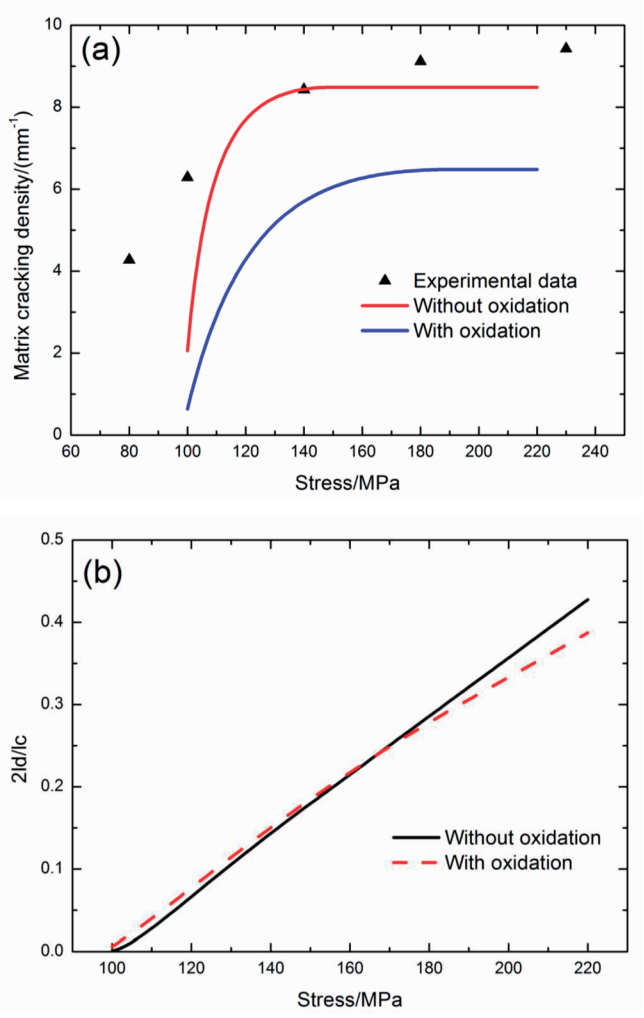

Fig. 9: The experimental and theoretical matrix multiple cracking of unidirectional C/SiC composite.

1. C/SiC composite

For C/SiC composite without oxidation, the matrix cracking evolution starts from the applied stress of 100 MPa and approaches saturation at the applied stress of 220 MPa; the matrix cracking density increases from 2.0/mm to the saturation value of 8.5/mm; and the fiber/matrix interface debonded length increases from 0.05 % at 100 MPa to 42.7 % at 220 MPa. With oxidation, the matrix cracking density increases from 0.6/mm at 100 MPa to 6.4/mm at 190 MPa; and the fiber/matrix interface debonding ratio increases from 0.6 % at 100 MPa to 38 % at 220 MPa, as shown in Fig. 9. The optical micrograph of the multiple matrix cracking on the edge surface is shown in Fig. 10.

Table 1: The material properties of SiC/CAS, SiC/borosilicate and mini-SiC/SiC composites.

Items	C/SiC	SiC/CAS [19]	SiC/borosilicate [24]	mini-SiC/SiC [38]
E_f/(GPa)	230	190	230	160
E_m/(GPa)	350	90	60	190
V_f	0.42	0.34	0.31	0.25
r_f/(μm)	3.5	7.5	8	6.5
α_f/(10^{-6}/K)	-0.38	3.3	3.1	3.1
α_m/(10^{-6}/K)	2.8	4.6	3.25	4.6
τ_i/(MPa)	7.8	10	7.6	15
ζ_d/(J/m^2)	1.2	0.4	0.2	0.4

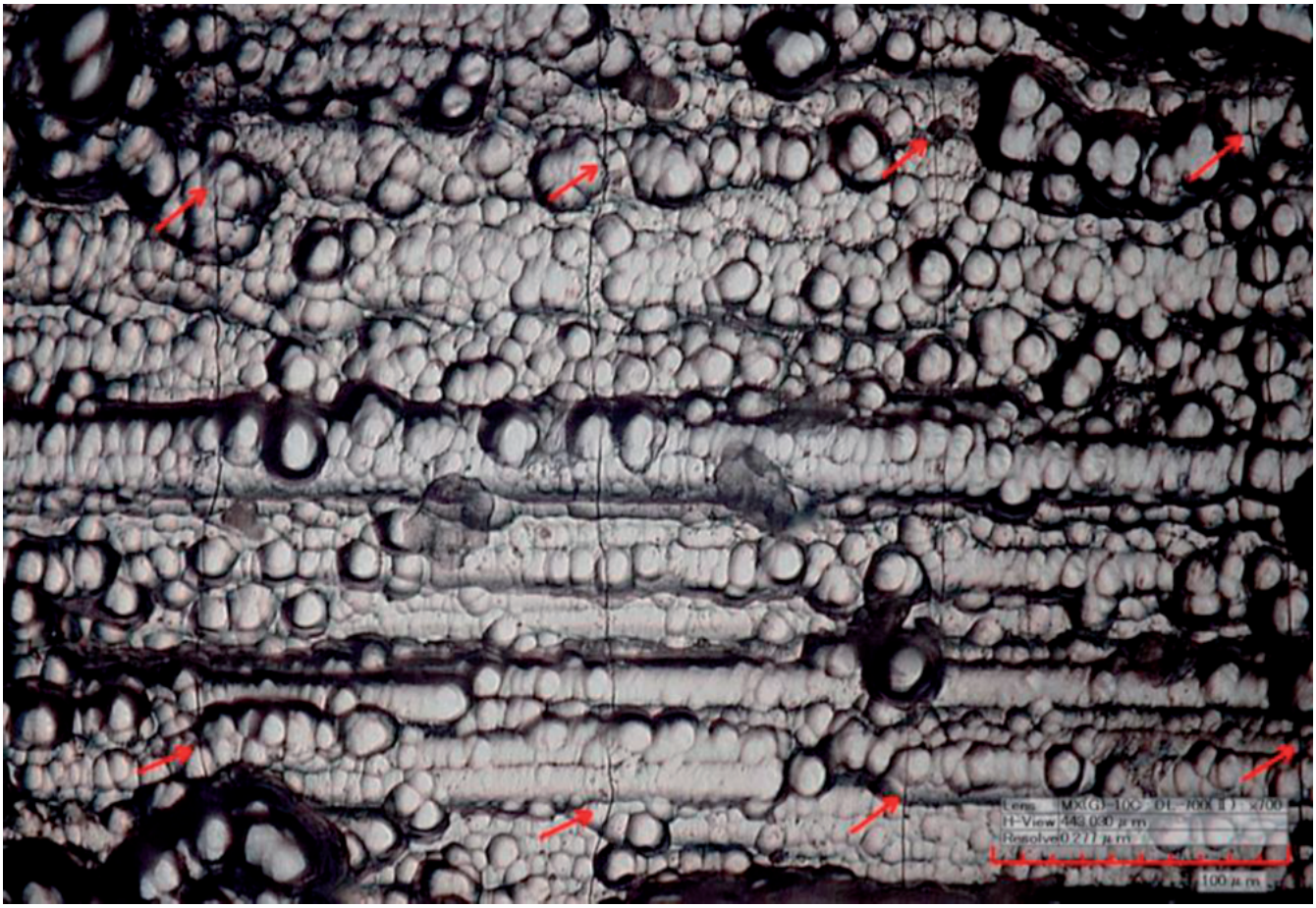

Fig. 10: The matrix multiple cracking of failed tensile specimen observed under an optical microscope.

2. *SiC/CAS composite*

For SiC/CAS composite without oxidation, the matrix cracking evolution starts from the applied stress of 140 MPa and approaches saturation at the applied stress of 288 MPa; the matrix cracking density increases from 0.7/mm to the saturation value of 7/mm; and the fiber/matrix interface debonded length increases from 0.7 % at 160 MPa to 79 % at 360 MPa. With oxidation, the matrix cracking density increases from 0.13/mm at 160 MPa to 4.8/mm at 332 MPa; and the fiber/matrix interface debonding ratio increases from 0.86 % at 160 MPa to 72 % at 360 MPa, as shown in Fig. 11.

3. *SiC/borosilicate composite*

For SiC/borosilicate composite without oxidation, the matrix cracking evolution starts from the applied stress of 220 MPa and approaches saturation at the applied stress of 360 MPa; the matrix cracking density increases from 0.2/mm to the saturation value of 6.5/mm; and the fiber/matrix interface debonded length increases from 0.8 % at 220 MPa to 82 % at 420 MPa. With oxidation, the matrix cracking density increases from 0.1/mm at 220 MPa to 4.4/mm at 414 MPa; and the fiber/matrix interface debonding ratio increases from 0.92 % at 220 MPa to 78 % at 420 MPa, as shown in Fig. 12.

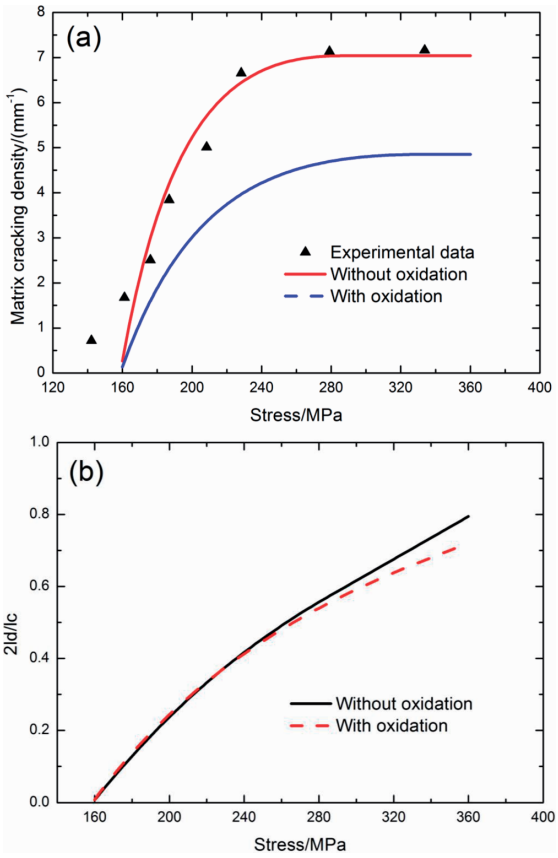

Fig. 11: (a) The experimental and theoretical matrix cracking density versus applied stress curves; (b) the fiber/matrix interface debonded ratio ($2l_d/l_c$) versus applied stress curves of unidirectional SiC/CAS composite with/without oxidation.

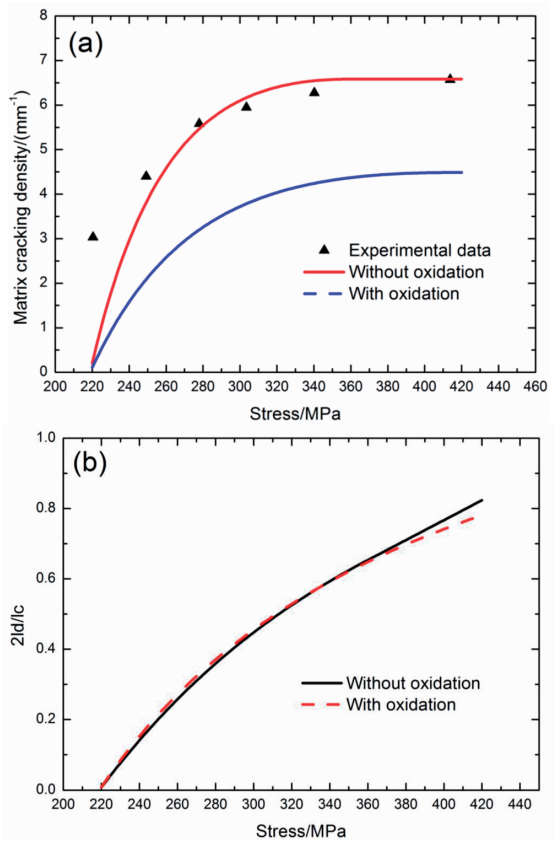

Fig. 12: (a) The experimental and theoretical matrix cracking density versus applied stress curves; (b) the fiber/matrix interface debonded ratio ($2l_d/l_c$) versus applied stress curves of unidirectional SiC/borosilicate composite with/without oxidation.

4. Mini-SiC/SiC composite

For mini-SiC/SiC composite without oxidation, the matrix cracking evolution starts from the applied stress of 135 MPa and approaches saturation at the applied stress of 250 MPa; the matrix cracking density increases from 0.4/mm to the saturation value of 2.4/mm; and the fiber/matrix interface debonded length increases from 1 % at 135 MPa to 98 % at 330 MPa. With oxidation, the matrix cracking density increases from 0.06/mm at 135 MPa to 2.2/mm at 260 MPa; and the fiber/matrix interface debonding ratio increases from 0.99 % at 135 MPa to 91.8 % at 330 MPa, as shown in Fig. 13.

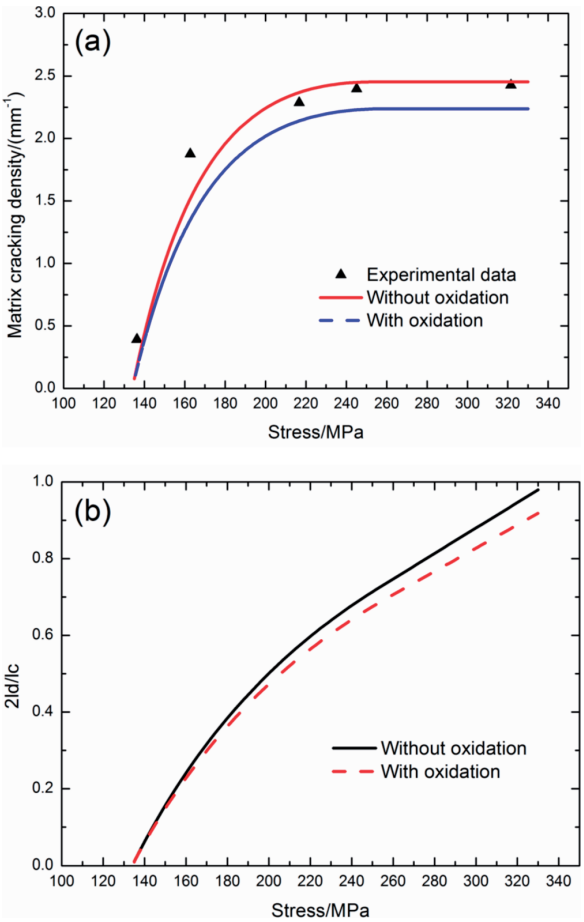

Fig. 13: (a) The experimental and theoretical matrix cracking density versus applied stress curves; (b) the fiber/matrix interface debonded ratio ($2l_d/l_c$) versus applied stress curves of mini-SiC/SiC composite with/without oxidation.

V. Conclusions

In this paper, the effect of fiber/matrix interface oxidation on matrix multi-cracking evolution of fiber-reinforced CMCs has been investigated using the critical matrix strain energy criterion. The shear-lag model combined with the fiber/matrix interface oxidation model and fiber/matrix interface debonding criterion has been adopted to analyze the fiber and matrix axial stress distribution inside the damaged composite. The relationships between the matrix multi-cracking, fiber/matrix interface debonding and oxidation have been established. The effects of fiber volume fraction, fiber/matrix interface shear stress, fiber/matrix

interface debonded energy, oxidation temperature and oxidation time on the stress-dependent matrix multi-cracking development have been discussed. Comparisons of matrix multi-cracking evolution with/without oxidation have been analyzed. The experimental matrix multi-cracking development of unidirectional C/SiC, SiC/CAS, SiC/borosilicate and mini-SiC/SiC composites with/without oxidation have been predicted.

(1) With increasing fiber volume fraction, the first matrix cracking stress, matrix saturation cracking stress and matrix cracking density increase; the fiber/matrix interface debonded length and interface debonding ratio decrease; and the interface oxidation ratio increases.
(2) With increasing fiber/matrix interface shear stress of τ_i, the first matrix cracking stress, matrix saturation cracking stress and matrix cracking density increase; the fiber/matrix interface debonded length and interface debonding ratio decrease; and the fiber/matrix interface oxidation ratio increases.
(3) With increasing fiber/matrix interface shear stress of τ_f, the matrix cracking density increases; the fiber/matrix interface debonded length decreases; and the fiber/matrix interface oxidation ratio increases.
(4) With increasing fiber/matrix interface debonded energy, the matrix cracking density increases; the fiber/matrix interface debonded length and interface debonding ratio decrease; and the fiber/matrix interface oxidation ratio increases.
(5) With increasing oxidation temperature and time, the matrix cracking density decreases; the fiber/matrix interface debonded length increases; and the fiber/matrix interface oxidation ratio increases.

Acknowledgements

The work reported here is supported by the Fundamental Research Funds for the Central Universities (Grant No. NS2016070). The author also wishes to thank two anonymous reviewers and editors for their helpful comments on an earlier version of the paper.

References

1 Christin, F.: Design, fabrication, and application of thermostructural composites (TSC) like C/C, C/SiC and SiC/SiC composites, Adv. Eng. Mater., **4**, 903–912, (2002).

2 Naslain, R.: Design, preparation and properties of non-oxide CMCs for application in engines and nuclear reactors: an overview, Compos. Sci. Technol., **64**, 155–170, (2004).

3 Schmidt, S., Beyer, S., Knabe, H., Immich, H., Meistring, R., Gessler, A.: Advanced ceramic matrix composite materials for current and future propulsion system applications, Acta Astronaut., **55**, 409 – 420, (2004).

4 DiCarlo, J.A., Roode, M.: Ceramic composite development for gas turbine hot section components. Proceedings of the ASME Turbo Expo: Power for Land, Sea and Air, **2**, 221 – 231, (2006).

5 Stephen, T.: General Electric primes CMC for turbine blades. Flight International, 2010. http://www.flightglobal.com/news/articles/general-electric-primes-cmc-for-turbine-blades-349834/

6 Zhang, L.T., Cheng, L.F., Luan, X.G., Mei, H., Xu, Y.D.: Environmental performance testing system for thermostructure materials applied in aeroengines, Key Eng. Mater., **313**, 183 – 190, (2006).

7 Watanabe, F., Nakamura, T., Shinohara, K.: The application of ceramic matrix composite to low pressure turbine blade, Proceedings of ASME Turbo Expo 2016: Turbomachinery Technical Conference and Exposition, Seoul, South Korea, June 13 – 17 2016.

8 Cox, B.N., Marshall, D.B.: Crack initiation in fiber-reinforced brittle laminates, J. Am. Ceram. Soc., **79**, 1181–1188, (1996).

9 Sevener, K.M., Tracy, J.M., Chen, Z., Kiser, J.D., Daly, S.: Crack opening behavior in ceramic matrix composites, J. Am. Ceram. Soc., **100**, 4734–4747, (2017).

10 Filipuzzi, L., Camus, G., Thebault, J., Naslain, R.: Oxidation, mechanics and kinetics of 1D-SiC/SiC composite materials: I an experimental approach, J. Am. Ceram. Soc., **77**, 459–466, (1994).

11 Lamouroux, F., Jouin, J.M., Naslain, R.: Kinetics and mechanics of oxidation of 2D woven C/SiC composites: II, theoretical approach, J. Am. Ceram. Soc., **77**, 2058–2068, (1994).

12 Verrilli, M.J., Opila, E.J., Calomino, A., Kiser, J.D.: Effect of environment on the stress-rupture behavior of a carbon-fiber-reinforced silicon carbide ceramic matrix composite, J. Am. Ceram. Soc., **87**, 1536–1542, (2004).

13 Halbig, M.C., McGuffin-Cawley, J.D., Eckel, A.D., Brewer, D.N.: Oxidation kinetics and stress effects for the oxidation of continuous carbon fibers within a microcracked C/SiC ceramic matrix composite, J. Am. Ceram. Soc., **91**, 519–526, (2008).

14 Li, L.B.: Modeling matrix cracking of fiber-reinforced ceramic-matrix composites under oxidation environment at elevated temperature, Theor. Appl. Fract. Mech., **87**, 110–119, (2017).

15 Smith, C.E., Morscher, G.N., Xia, Z.H.: Monitoring damage accumulation in ceramic matrix composites using electrical resistivity, Scripta Mater., **59**, 463–466, (2008).

16 Simon, C., Rebillat, F., Herb, V., Camus, G.: Monitoring damage evolution of $SiC_f/[Si\text{-}B\text{-}C]_m$ composites using electrical resistivity: crack density-based electromechanical modeling, Acta mater., **124**, 579–587, (2017).

17 Gowayed, Y., Ojard, G., Santhosh, U., Jefferson, G.: Modeling of crack density in ceramic matrix composites, J. Compos. Mater., **49**, 2285–2294, (2015).

18 Parthasarathy, T.A., Cox, B., Surde, O., Przybyla, C., Cinibulk, M.K.: Modeling environmentally induced property degradation of SiC/BN/SiC ceramic matrix composites, J. Am. Ceram. Soc., **101**, 973–997, (2018).

19 Pryce, A.W., Smith, P.A.: Behavior of unidirectional and crossply ceramic matrix composites under quasi-static tensile loading, J. Mater. Sci., **27**, 2695–2704, (1992).

20 Aveston, J., Cooper, G.A., Kelly, A.: Single and multiple fracture. The Properties of Fiber Composites, Conference on Proceedings. National Physical Laboratory. Guildford: IPC Science and Technology Press, 15–26, (1971).

21 Beyerle, D.S., Spearing, S.M., Zok, F.W., Evans, A.G.: Damage and failure in unidirectional ceramic matrix composites, J. Am. Ceram. Soc., **75**, 2719–2725, (1992).

22 Holmes, J.W., Cho, C.D.: Experimental observations of frictional heating in fiber-reinforced ceramics, J. Am. Ceram. Soc., **75**, 929–938, (1992).

23 Kuo, W.S., Chou, T.W.: Multiple cracking of unidirectional and cross-ply ceramic matrix composites, J. Am. Ceram. Soc., **78**, 745–755, (1995).

24 Okabe, T., Komotori, J., Shimizu, M., Takeda, N.: Mechanical behavior of SiC fiber reinforced brittle-matrix composites, J. Mater. Sci., **34**, 3405–3412, (1999).

25 Morscher, G.N., Singh, M., Kiser, J.D., Freedman, M., Bhatt, R.: Modeling stress-dependent matrix cracking and stress-strain behavior in 2D woven SiC fiber reinforced CVI SiC composites, Compos. Sci. Technol., **67**, 1009–1017, (2007).

26 Morscher, G.N., Gordon, N.A.: Acoustic emission and electrical resistance in SiC-based laminate ceramic composites test-

ed under tensile loading, J. Eur. Ceram. Soc., **37**, 3861–3872, (2017).

[27] Racle, E., Godin, N., Reynaud, P., Fantozzi, G.: Fatigue lifetime of ceramic matrix composites at intermediate temperature by acoustic emission, Materials, **10**, 658, (2017).

[28] Solti, J.P., Mall, S., Robertson, D.D.: Modeling damage in unidirectional ceramic-matrix composites, Compos. Sci. Technol., **54**, 55–66, (1995).

[29] Rajan, V.P., Zok, F.W.: Matrix cracking of fiber-reinforced ceramic composites in shear, J. Mech. Phys. Solids, **73**, 3–21, (2014).

[30] Casas, L., Martinez-Esnaola, J.M.: Modelling the effect of oxidation on the creep behavior of fiber-reinforced ceramic matrix composites, Acta mater., **51**, 3745–3757, (2003).

[31] Budiansky, B., Hutchinson, J.W., Evans, A.G.: Matrix fracture in fiber-reinforced ceramics. J. Mech. Phys. Solids, **34**, 167–189, (1986).

[32] Gao, Y.C., Mai, Y., Cotterell, B.: Fracture of fiber-reinforced materials, J. Appl. Math. Phys., **39**, 550 – 572, (1988).

[33] Curtin, W.A.: Theory of mechanical properties of ceramic-matrix composites, J. Am. Ceram. Soc., **74**, 2837–2845, (1991).

[34] Phoenix, S.L., Raj, R.: Scalings in Fracture Probabilities for a Brittle Matrix Fiber Composite. Acta metal mater., **40**, 2813–2828, (1992).

[35] Li, L.B.: Synergistic effects of fiber debonding and fracture on matrix cracking in fiber-reinforced ceramic-matrix composites, Mater. Sci. Eng. A, **682**, 482–490, (2017).

[36] Li, L.B., Song, Y.D., Sun, Y.C.: Modeling the tensile behavior of unidirectional C/SiC ceramic-matrix composites, Mech. Compos. Mater., **49**, 659–672, (2014).

[37] Li, L.B., Song, Y.D., Sun, Y.C.: Modeling the tensile behavior of cross-ply C/SiC ceramic-matrix composites, Mech. Compos. Mater., **51**, 359–376, (2015).

[38] Zhang, S., Gao, X., Chen, J., Dong, H., Song, Y.: Strength model of the matrix element in SiC/SiC composites, Mater. Design, **101**, 66–71, (2016).